scientific reports

Check for updates

OPEN

# Development, characterization and biological studies of Mn-doped ZnO/Ti biomaterials for regenerative medicine

Dario Morganti[1,7], Domenico Franco[1,7], Maria Giovanna Rizzo[1,7], Laura Maria De Plano[1], Antonella Iaconis[1], Giovanna Calabrese[1], Marco Sebastiano Nicolò[1], Giovanna De Luca[1]✉, Carmelo Corsaro[2], Enza Fazio[2], Fortunato Neri[2], Matteo Giunta[3], Antonio Alessio Leonardi[4], Giuseppe Nicotra[5] & Sabrina Conoci[1,4,6]✉

**Bone disease diseases massively affect the world population, with more than two million of surgeries performed worldwide every year. Bone has limited capability to repair very large defects and the use of engineered biomaterials isa mandatory but some clinical issues are observed like rejection and possible infections. Therefore, the development of new biomaterials promoting bone tissue repair and prevent post-surgery infections represents one of the main challenge in regenerative medicine. Titanium is the most used material for implants but it not free from infections. Therefore the modification of Ti surface could represent a valuable strategy to improve both antibacterial and osteo-inductive properties. In this work, we developed a Mn-doped ZnO/Ti biomaterial and evaluated its ability to prevent infections, preserving the osteo-integration. Results indicate that the biomaterial is very effective in antibacterial activity with a bacterial reduction of more than 80% in the case of *Staphylococcus aureus*, and of 44.4% and 53.6% in the case of *Pseudomonas aeruginosa*, while maintaining both biocompatibility and the ability to promote osteogenic differentiation, as confirmed by upregulation of key genes (ALP, IBSP, SPARC) in human osteoblasts. This paves the way for a new class of biomaterials for regenerative medicine applications.**

**Keywords** Mn-doped ZnO/Ti biomaterial, Surface functionalization, Antibacterial activity, Bone tissue, Osteo-integration

Nanotechnologies have received great attention in the development of new materials for bone tissue engineering, offering multidisciplinary approaches, including physics, chemistry, engineering, physiology, and medicine[1]. Rapid progress in nanotechnology for biomaterials contributes to formulating novel strategies for innovative and functional bone grafts and implants. Nowadays, bone defect repair is one of the most common procedures, with more than 2 million bone surgeries performed annually worldwide[2–5] due to trauma, congenital anomalies, and tissue resection due to cancer and osteoporosis[6]. Since the bone ability to repair very large defects is limited, several biomaterials have been developed in the last few years using advanced materials science and stem cell technologies to achieve this goal and face the challenges of reducing adverse side effects, such as post-surgery bacterial infections[7–9]. However, most implantable device surfaces favor the colonization of bacteria, which are often difficult to remove and exhibit the onset of high antibiotic resistance[10,11], creating a relevant clinical issue[12].

In its pure or alloy form[13,14], titanium is the most commonly used material for manufacturing permanent artificial implants in vivo, thanks to its excellent mechanical[13,15], chemical[16,17], and biocompatible[14,18,19]

[1]Department of Chemical, Biological, Pharmaceutical and Environmental Sciences (ChiBioFarAm), University of Messina, Viale F. Stagno d'Alcontres 31, 98166 Messina, Italy. [2]Department of Mathematical and Computational Sciences, Physics Science and Earth Science, University of Messina, Viale F. Stagno d'Alcontres 31, 98166 Messina, Italy. [3]MTOrtho, Via Fossa Lupo, 95025 Aci San'Antonio, CT, Italy. [4]LAB Sense Beyond Nano - URT Department of Sciences Physics and Technologies of Matter (DSFTM) CNR, Viale F. Stagno d'Alcontres 31, 98166 Messina, Italy. [5]Istituto per la Microelettronica e Microsistemi, Consiglio Nazionale delle Ricerche (CNR-IMM), Catania, Italy. [6]Department of Chemistry "Giacomo Ciamician", University of Bologna, Via Selmi 2, 40126 Bologna, Italy. [7]Morganti Dario, Franco Domenico and Rizzo Maria Giovanna equally contributed to this work. ✉email: giovanna.deluca@unime.it; sabrina.conoci@unime.it

properties. Both *in vivo* and *in vitro* studies showed an effective osteointegration of Ti, with bone tissues bonded efficiently to the implants, as demonstrated, among other things, by human osteoblast cells' response (MG-63)[20].

However, Ti implants cannot prevent infections since their surfaces can provide a good handle for the pathogenic bacteria forming hazardous biofilms. This may lead to failure of surgical procedures with negative patient compliance and economic impact on the healthcare system.

Gram-positive strains, mainly belonging to the Staphylococci, are the mainly emerging bacteria following implant surgery, whereas Gram-negative ones (like *P.aeruginosa*) are less frequent as a cause of infections[10]. Specifically, *Staphylococcus aureus* (Gram-positive) represents the most frequent vector of infections caused by orthopedic surgery[21].

Recent studies reported the possibility of minimizing bacterial adhesion by modifying titanium surfaces with organic or inorganic coatings[22,23]. However, organic materials have several limitations regarding stability and compatibility with industrial sterilization processes, which may limit their diffusion in biomedical fields. On the contrary, inorganic materials can represent a promising solution due to their higher chemical stability and thermal resistance. Recently, the possibility of using metal-based nanoparticles (NPs) as antibacterial agents has been widely studied[24,25]. The mechanism of their antibacterial activity mainly involves ion leaching/dissolution, later interacting with the cell membrane or diffusing inside them and interacting with cellular components like structural proteins, enzymes, and nucleic acids[26–28]. Induction of reactive oxygen species (ROS) by Fenton-type or Haber–Weiss-type reactions is also involved in bacterial cell disruption[29].

Zinc oxide (ZnO)-based NPs have recently provided a relevant antibacterial effect[30]. Their doping with other elements, e.g., with Mn, can open novel opportunities for new implantable materials with both enhanced bone repair properties and effective antibacterial capabilities[31]. In addition, zinc oxide nanoparticles have been shown to improve bone growth and promote osteoblast proliferation when incorporated with hydroxyapatite (HA), improving bone mineral matrix secretion (98%) and osteoblast proliferation[32].

Mn plays an essential role as a micronutrient to promote living organisms' metabolism, growth, and reproduction[33–35]. Furthermore, it is a fundamental element for promoting the growth of connective tissue and bones[36]. Implants doped with Mn have demonstrated promising results in bone regeneration, with Mn-doped bioactive glass supporting osteoblast proliferation and spreading, indicating its potential as a bone regeneration material[20]. In a recent work, we described an alternative nano-functionalization of titanium scaffolds with colloidal ZnO and Mn-doped ZnO NPs by a wet chemistry co-precipitation method[37]. Although an efficient bactericidal activity was obtained on both planktonic and sessile cells, however preliminary data of cytotoxic evaluation, crucial for the real use, was shown some limitations in terms of biocompatibility. Recent evidence suggests that Mn incorporation can also modulate osteoblastic gene expression, promoting cell proliferation and early differentiation essential for effective osseointegration.

In this work, we developed a new formulation of Mn-doped ZnO/Ti biomaterial and evaluated both the antibacterial activity towards *P.aeruginosa* and *S.aureus* and the biocompatibiliy against Human Fetal Osteoblasts. In addition we perfomed gene expression of alkaline phosphatase (ALP), bone sialoprotein (IBSP), and osteonectin (SPARC) that highlights for the fisrt time the ability of this material to provide osteo-integration, while mantaing excellent antibacterial properties, making it suitable for real-world applications.

## Results and discussions

ZnO NPs and Mn-ZnO NPs were synthesized in a few steps starting from metal acetate precursors (see scheme in S1). SEM analysis performed on both ZnO NPs and Mn-ZnO NPs deposited onto a commercial n-doped (1–5 Ω·cm) (100)-silicon substrate showed nanostructures with diameters lower than 10 nm (see Figure S2a-c) without any distinguishable variation between doped and undoped NPs. This dimension renders to obtain a size distribution by SEM complex and non-reliable. For this reason, the size distribution of ZnO and Mn-ZnO NPs in DMSO suspension was characterized by High Resolution-Transmission Electron Microscopy (HR-TEM), as reported in Fig. 1. The presence of both Mn and Zn was initially attested by a Rutherford Backscattering Spectrometry (RBS) analysis performed on Mn-doped Zn NPs (Figure S3d). RBS is a reliable approach for thin films, but fitting an RBS spectrum of a NPs distribution is extremely complex. Moreover, as RBS is sensitive to the atomic number (Z), quantitatively distinguishing Mn (Z = 25) and Zn (Z = 30) is not reliable in this context (see Supplementary Information for more details). Hence, an Energy Dispersive X-ray Analysis (EDX) was performed to attest the Mn presence (Fig. 1).

Figure 1a allows to distinguish clearly the ZnO NPs, which are characterized by a clear crystalline structure showing the crystallographic lattice planes. The NP size distribution was obtained by analyzing several images acquired at different points of the samples, and the obtained histogram was reported in Fig. 1b with an average dimension of (4.7 ± 0.5) nm. As expected, the EDX spectrum of ZnO NPs in Fig. 1c confirms the presence of a sample composed only of oxygen and zinc. In particular, the signal at 0.52 keV is attributable to oxygen, while the signals at 1.01 keV and 8.65 keV are attributable to the $L$ ($L_{\alpha1}$, $L_{\alpha2}$, $L_{\beta2}$) and $K$ ($K_{\alpha1}$, $K_{\alpha2}$) Zn transitions, respectively[38]. The intense peak at 9.6 keV is a convolution of Au-$L_{\alpha1}$ and Au-$L_{\alpha2}$ (gold sample holder grid) and the $K_{\beta1}$ and $K_{\beta2}$ Zn contributions.

Figure 1d reports the Mn-ZnO NPs HR-TEM image showing the NPs' crystalline structure. The size distribution of Mn-ZnO NPs NPs is reported in Fig. 1e and, in this case, fitted by a Gaussian curve, obtaining an average diameter of (4.5 ± 0.5) nm. The size decrease compared to the undoped ones is negligible considering the error associated to the average diameters of ZnO NPs and Mn-ZnO NPs. The presence of Mn was detected and confirmed by EDX spectroscopy (Fig. 1f) despite its low concentration. The EDX analysis allows us to identify the same signals already observed with ZnO NPs plus the Mn contribution, namely, the peaks at 5.9 keV and 6.44 keV that are attributable to the Mn-$K_{\alpha}$ and Mn-$K_{\beta}$ transitions, respectively (see the inset in Fig. 1f).

Electron Energy Loss Spectroscopy (EELS) experiments coupled with TEM characterization were performed on both NPs to confirm the presence of Mn and to determine its oxidation state. The ZnO and Mn-ZnO NPs'

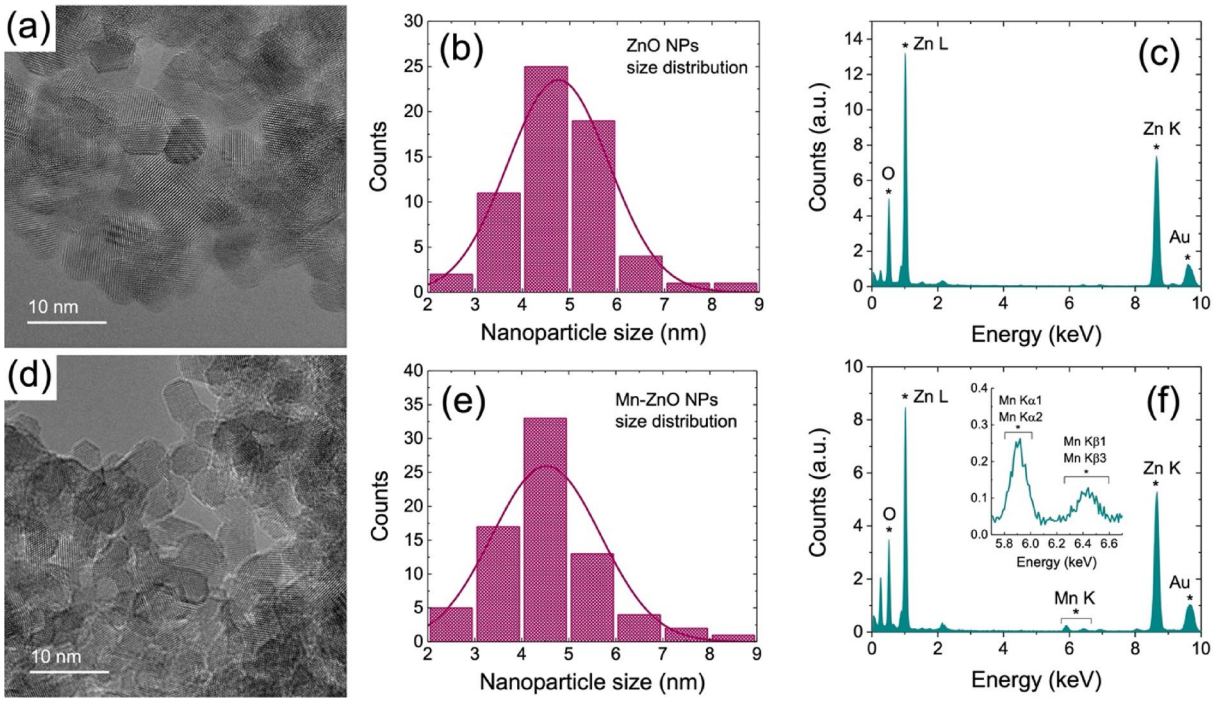


**Fig. 1**. Structural characterization of ZnO NPs (**a**–**c**) and Mn-ZnO NPs (**d**-**f**). High Resolution Transmission Electron Microscopy (**a**, **d**). Nanoparticle size distribution (**b**, **d**). EDX spectroscopy (**c**, **f**); the magnification of Mn-K signals is shown as inset in (**f**).

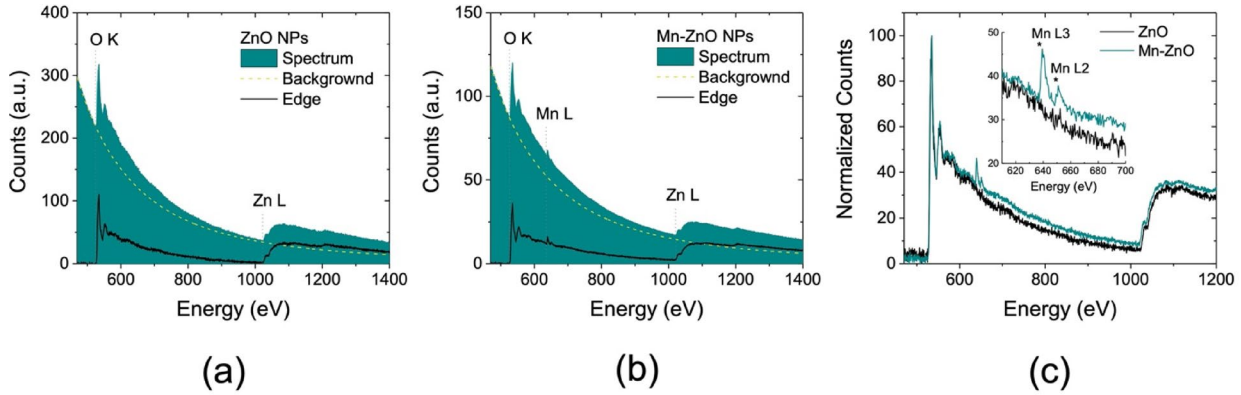


**Fig. 2**. Electron Energy Loss Spectroscopy of ZnO NPs (**a**) and Mn-ZnO NPs (**b**). (**c**) ZnO (solid black line) and Mn-ZnO (solid green line) normalized edges; the magnification of Mn-$L_3$ and Mn-$L_2$ signals is shown as inset in (**c**).

EELS spectra are shown in Fig. 2a,b, respectively. In both graphs, it is possible to observe the edges of oxygen at 535 eV (O-*K*), and those of zinc at 1020 eV (Zn-$L_3$), 1145 eV (Zn-$L_2$), and 1195 eV (Zn-$L_1$) emerging from the background plasmon tail (dotted yellow line). Figure 2c shows the edge spectra of ZnO (black line) and Mn-ZnO NPs (green line) normalized to their O-*K* lines. Here, the Mn signals at 640 eV (Mn-$L_3$) and 650 eV (Mn-$L_2$) are clearly visible and distinguishable in the inset, confirming once again the presence of Mn atoms. Moreover, the peak position of the $L_3$ and $L_2$ lines together with a 2.8 $L_3/L_2$ ratio suggests the presence of $Mn^{2+}$ ions[39] and, therefore, its function as a doping agent in replacing $Zn^{2+}$ ions in the crystal lattice.

Figure 3 shows the FT-IR spectra acquired on ZnO and Mn-ZnO NPs. The observed band centered at around 650 and 850 $cm^{-1}$ is ascribed to Mn–O and Zn–O–Mn stretching modes and Mn ions defect states[40]. In addition, the broad absorption in the 3350–3650 $cm^{-1}$ range is attributed to the –OH groups of $H_2O$, indicating the presence of water absorbed on the surface of ZnO nanostructures. The weak absorption bands at about 1520 and 1385 $cm^{-1}$ are due to the symmetric and asymmetric C=O stretching bond[41], probably due to the presence of the acetate counterions as impurities or capping species. The deformation bands of C=O can also be observed around 850–980 $cm^{-1}$[42]. Overall, substituting Mn ion into ZnO host material induces lattice distortion due to

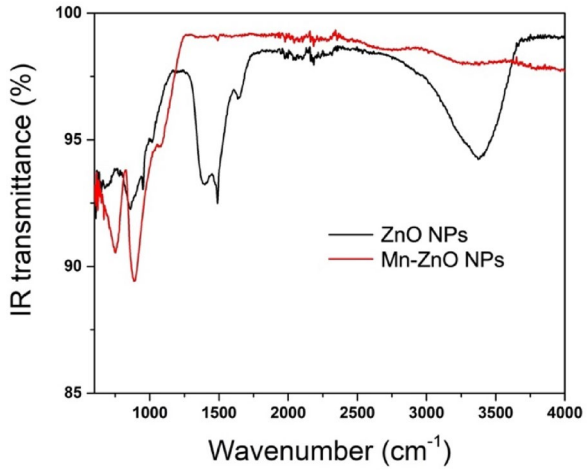


**Fig. 3**. FT-IR spectra of ZnO (black line) and Mn-ZnO (red line) NPs suspension.

the difference in the radii of pristine $Zn^{2+}$ and dopant $Mn^{2+}$ (0.80 Å). Raman spectra also suggest that $Mn^{2+}$ ions act as dopants in the ZnO lattice[37].

To confirm the Mn-doping, extinction spectra were recorded according to what reported in the literature by Karamat et al. that show a blue shift in the absorption spectra of ZnO caused by the Mn-doping[43]. The spectra exibits an intense absorption in the region between 300 and 400 nm and photoluminescence (PL) at ~ 600 nm (see Figure S3). The blue shift in the edge of the absorption maximum ($\Delta\lambda = -4$ nm) suggest the correct Mn incorporation in the ZnO NPs, where $Mn^{2+}$ ions replace $Zn^{2+}$ within lattice (Burstein-Moss effect)[43–45]. Mn-doping influences the optical properties of the NPs, causing a shift in the absorption maximum, PL quenching, and the energy band gap varying from 3.46 eV for ZnO to 3.44 eV for Mn-doped ZnO (Figure S3).

The above-described Mn-doped ZnO NPs were used to functionalize trabecular Ti scaffolds by dipping (see Figure S4). Figure 4 shows SEM images at different resolutions of (i) pristine (a and d), (ii) ZnO-functionalized (b and e), and (iii) Mn-ZnO-functionalised (c and f) Ti scaffolds. The latter samples are totally and uniformly covered by ZnO and Mn-ZnO NPs. The surface morphology of the ZnO NPs-functionalized Ti scaffolds is characterized by a dense forest of nanosheets growing attached to the Ti by their thin edges, with the larger 2D crystal faces oriented almost perpendicularly to the Ti surface. The approximate lateral size of these ZnO 2D nanostructures falls in the submicron range, whereas the nanosheets' approximate thickness lies below 50 nm. In the presence of Mn doping, the nanosheets still form but are less dense and have a slightly larger lateral size while keeping the approximate thickness below 50 nm.

The estimated percentages of the atomic species detected by EDX are also shown in Fig. 4. The most abundant elements are Ti and O, while the reduction in the relative Zn amount in the samples containing Mn further indicates that Mn ions substituted Zn ones. The Al signal is due to the presence of this atom in the Ti scaffold alloy (Ti6Al4V).

In order to assess the bactericidal effect of the nano-functionalized scaffolds, Gram-positive *Staphylococcus aureus* (*S. aureus*) ATCC29213 and Gram-negative *Pseudomonas aeruginosa* (*P. aeruginosa*) ATCC27853 were used since they are among the most common pathogens associated with prosthetic infections[46,47]. Once infections occur, bacteria can be present in the tissue far from or in contact with the scaffold surface. In the first case, bacterial cells are free-floating (planktonic cells) in the medium and do not interact with the prosthetic surfaces. The antibiotic treatments of planktonic cells are generally favored due to their greater susceptibility[48]. Otherwise, when bacterial cells are constrained near/by the surface and under favorable physicochemical conditions, a small community of cells will start adhering and growing (sessile cells)[49]. The progression of the latter event will lead to the colonization of the entire surface by mono or mixed bacterial species, with the production and maturation of a biofilm that will lead to the same species having a lower susceptibility to biocidal treatments[50]. For these reasons, the bactericidal effect was mainly evaluated by looking at the eradication of sessile cells by the different nanocoatings. Figure 5 shows the results of bactericidal activity on the sessile cells bound to the NPs/Ti scaffold surfaces.

Concerning *S. aureus*, a reduction of cells of more than 80% was observed for all treatments, indicating a high susceptibility of the Gram-positive strain to the metal oxide nanocoatings compared to untreated Ti scaffolds (Fig. 5a). Specifically, a reduction of 80.7% and 87.4% was found for the coatings with ZnO NPs at 1:100 and 1:50 dilution. An even more significant bacterial reduction was observed when the ZnO NPs were doped with Mn (84% and 88.3% for dilution 1:100 and 1:50, respectively). No surface treatment significantly inhibited the planktonic cell growth (see Figure S5a).

As far as *P. aeruginosa* is concerned, our results indicated a scalar increment of bactericidal activity on adhered cells as a function of ZnO and Mn-ZnO concentrations (Fig. 5b). In fact, a reduction of 8.9% and 44.4% was found for ZnO NPs coverage obtained by dipping the scaffolds into 100- and 50-fold diluted suspensions of the NPs, respectively. In the case of Mn-doped ZnO nanocoatings, the bacterial reduction reached 16.6% and 53.6% for 100- and 50-fold dilutions. In this case, the viability of *P. aeruginosa* planktonic cells appeared also to

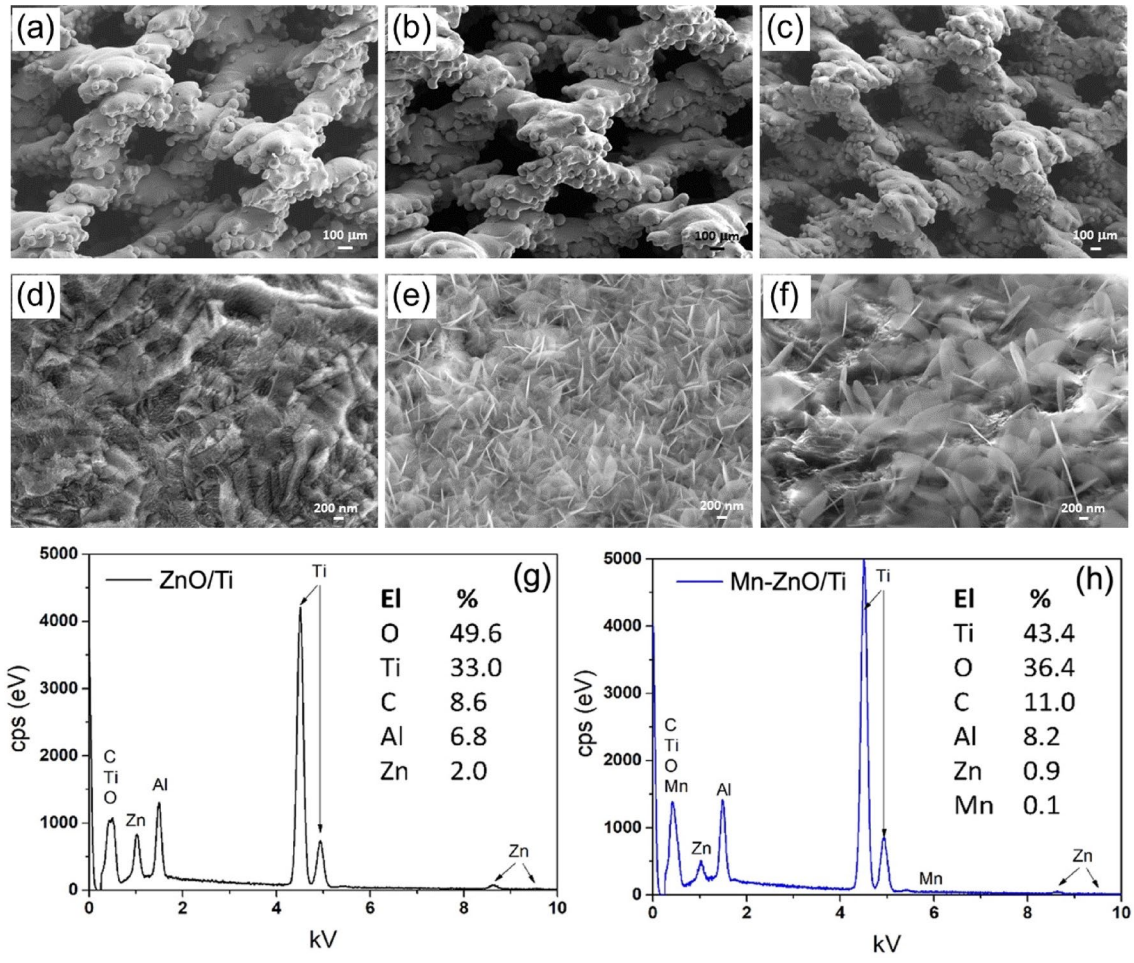


**Fig. 4**. SEM images acquired on pristine (**a**, **d**), ZnO-functionalized (**b**, **e**), and Mn-ZnO-functionalized (**e**, **f**) titanium scaffolds, together with. EDX spectra of ZnO/Ti (**g**) and Mn-ZnO/Ti (**h**).

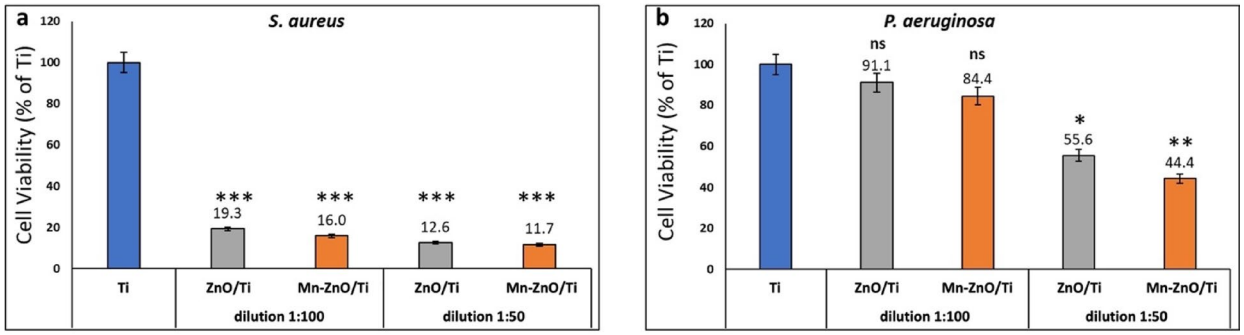


**Fig. 5**. Antimicrobial activity of titanium scaffolds coated with ZnO/Ti and Mn-ZnO NPs diluted 1:100 and 1:50 on sessile cells of *S. aureus* and *P. aeruginosa*. Data are shown as mean ± standard deviation. For ANOVA using Tukey's multiple comparison test, one (*), two (**), and three (***) asterisks identify *p*-values < 0.05, < 0.01, and < 0.001, respectively.

be affected by the metal oxide coatings obtained from 1:50 dilutions (Figure S5b). These samples also caused to a significant reduction in the pyocyanin production in the wells previously occupied by the scaffolds coated with ZnO and Mn-ZnO NPs (Fig. 6).

Pyocyanin is a characteristic blue-green pigment belonging to the group of secondary metabolites of phenazines, which are involved in the responses to alteration of cell redox states, enhancement of bacterial survival, and the regulation of alternative gene expression[51]. In addition, phenazines could be associated with

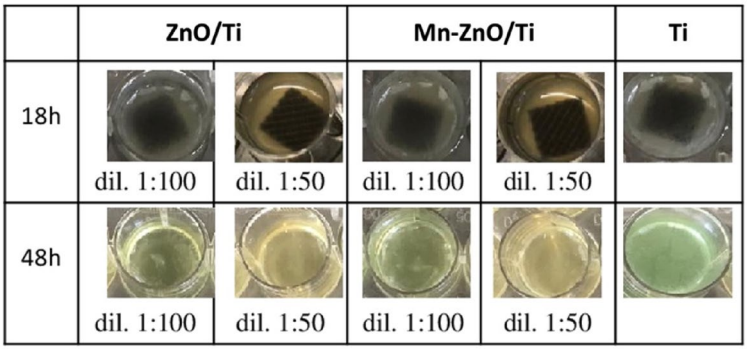


**Fig. 6**. Representative images of *P. aeruginosa* cultures with uncoated (Ti) and ZnO- and Mn-ZnO-coated scaffolds at 18 h and 48 h incubation.

the pathogen/host organisms interaction and infections with high morbidity and mortality[52,53]. Otherwise, their oxidation or molecular inactivation leads to an inhibition of different metabolic pathways associated with pathogenesis, such as those involved in the production and maturation of biofilms[54,55]. In fact, pyocyanin production in *P. aeruginosa* is controlled by a complex interplay of quorum sensing (QS) systems, including PqsR, RhlR, LasR, and IqsR[56–58]. PqsR and RhlR directly regulate the phenazine operon, driving pyocyanin biosynthesis, while LasR and IqsR exert indirect influence by promoting the activity of PqsR and RhlR, thereby contributing to the overall regulation of pyocyanin levels (Figure S6). The tight regulatory link between QS systems and pyocyanin also indirectly affects biofilm formation by modulating other virulence factors crucial for biofilm development. For instance, RhlR influences rhamnolipid production, which is essential for surface motility and initial biofilm adhesion, while PqsR modulates the quinolone signal molecules, enhancing biofilm cohesion. Therefore, inhibiting any one of these systems disrupts the downstream processes reliant on pyocyanin, demonstrating that the QS-pyocyanin-biofilm axis is critical for *P. aeruginosa* pathogenicity. Therefore, our results suggest that, although the presence of $Zn^{2+}$ and $Mn^{2+}$ ions was insufficient to drastically reduce the bacterial load, the metabolism of the Gram-negative strain was significantly altered, as indicated by the inhibition of pyocyanin production.

A literature study[59] shows that ZnO NPs can reduce the yield of pyocyanin synthesis and other virulence factors, such as proteases and hemolysin, in several *P. aeruginosa* strains, probably as a consequence of NPs accumulation inside their cells. Another example[60] states that ZnO NPs can inhibit the quorum sensing process by which *P. aeruginosa* globally modulates its transcriptional activity at the population level and regulates the biosynthesis of the virulence factors.

Consequently, the metal oxide coating should discourage the formation of mature biofilms on the scaffolds and increase the susceptibility of the strain to secondary antimicrobial treatments. On the other hand, bactericidal activity could be enhanced by increasing the amount of metal coating on the scaffolds. Indeed, when we used the 25-fold dilution during the dip coating process, the *P. aeruginosa* antibacterial assay indicated that the inhibition rates were significantly increased with a bacterial reduction of 66.7% and 73.3 for the ZnO and Mn-ZnO coatings, respectively (see Figure S7).

These findings indicate that, although the treatment is more effective with Gram-positive strains due to their higher susceptibility to the antibacterial action of $Zn^{2+}$ ions[61], a broad efficacy spectrum could be achieved by varying the metal oxides amount in the coatings. In addition, the presence of Mn within the coating enhances the antimicrobial activity of the surface against both the evaluated strains. Heavy metals such as Zn and Mn are essential micronutrients in numerous cell functions; however, they become toxic when accumulating over a given concentration[62,63]. On the other hand, bacterial strains can respond to heavy metals by the induction of several patterns of resistance genes arising from complex array of evolutionary[64]. Results from in silico *analysis* of genes involved in the resistance to $Zn^{2+}$ and $Mn^{2+}$ ions in *S. aureus* and *P. aeruginosa* are included in Table 1.

The analysis showed that the resistance genes for Zn(II) and Mn(II) ions are present in both the bacterial strains used in this work, often associated with other ions.

In *S. aureus* the best-characterized Zn resistance genes, cadA and cadC, are situated on plasmid systems. Specifically, cadA gene encodes for ATP energy-dependent exports from the cell, while cadC gene products a transcriptional repressor, released when metal ions bound the operator/promoter sequence[74]. Otherwise, in *P. aeruginosa* the genes identified to be involved in the Zn resistance, czrA and czrB, belong to the Resistance-Nodulation-Division superfamily (RND). These genes are located in the bacterial chromosome codify for ABC transporter systems responsible for both the efflux of drugs and metal ions[69]. The major evidence is that the resistance genes for Zn in *S. aureus* are located into plasmid structure, contrary to *P. aeruginosa* which brings the genes in the chromosome. These findings could explain the different susceptibility of two strains obtained in our experiments. Indeed, the presence in the chromosome make genes constitutive for *P. aeruginosa* which in presence of the ion can be activated. Contrary, *S. aureus* without the presence of plasmid have not possibility to block the toxicity of the Zn.

Other way, Mn resistance genes are located in the bacterial chromosome for both *S. aureus* and *P. aeruginosa* and are involved in the oxidative stress processes. Particularly, in *S. aureus* the PerR gene may act as a peroxide sensor, regulating the transcription of the genes encoding the oxidative stress resistance and the iron storage

| Ion metal | Bacteria | Gene name | Encoding for | BacMet ID | Family | Location | Description | Compound | References |
|---|---|---|---|---|---|---|---|---|---|
| Zn | *S. aureus* | cadC | Regulator | BAC0056 | Contains 1 HTH arsR-type DNA-binding domain | Plasmid pI258 | Metal-binding repressor for the cad operon | Cadmium (Cd), Bismuth (Bi), Zinc (Zn) | 65 |
| | | cadD | Enzyme | BAC0057 | CadD family | Plasmid pN315, Plasmid pLUH02 | Cadmium resistance permease. To date, only found in Gram-positive bacteria | Zinc (Zn), Cadmium (Cd) | 66,67 |
| | *P. aeruginosa* | czrA | Regulator | BAC0130 | RND superfamily | Chromosome | Repressor for the czr operon; part of the czrSRCBA resistance operon | | 68–70 |
| | | czrB | Efflux | BAC0131 | | | Involved in cadmium and zinc resistance; part of the czrSRCBA resistance operon | | 69,70 |
| | | fpvA | Porin | BAC0169 | Bacterial Porin family (GBP) superfamily. TonB-dependent receptor family | | Ferripyoverdine receptor A (fpvA); Receptor for the siderophore ferripyoverdine; Located in cell outer membrane | Manganese (Mn), Iron (Fe), Cobalt (Co), Zinc (Zn), Nickel (Ni), Copper (Cu), Cadmium (Cd), Gallium (Ga) | 71,72 |
| Mn | | sodB | Enzyme | BAC0706 | Iron/manganese superoxide dismutase family | | Fe-dependent superoxide dismutase; Destroys superoxide anion radicals | Hydrogen Peroxide (H2O2) [class: Peroxides] | 72 |
| | | sodA | Enzyme | BAC0705 | | | Mn-dependent superoxide dismutase; Destroys superoxide anion radicals | | |
| | *S. aureus* | perR | Regulator | BAC0310 | Fur family | | Manganese-dependent repressor: controls regulon of oxidative stress resistance and iron-storage | | 73 |

**Table 1**. Bioinformatic analysis of genes involved in metal resistance to Zn and Mn for *S. aureus* and *P. aeruginosa* strains.

proteins[73]. PerR is manganese-dependent, elevated iron concentrations lead to PerR regulon activation. In *P. aeruginosa*, superoxide dismutase (SOD) genes are first line of defence against potentially toxic levels of endogenous superoxide. These genes use ions, such as Mn and Fe, as cofactors to limit the damage due to oxygen free radicals, and they are involved in the pyocyanin biosynthesis in *P. aeruginosa*[75].

About gene FpvA, potentially activated in both metal resistance Zn and Mn in *P. aeruginosa*, is an outer membrane transporter involved in the pathway for Pyoverdine (PVD)–iron uptake from the extracellular medium into the periplasm. PVD is the major siderophore produced by *P. aeruginosa* for metals acquisition into bacterium periplasm, after that, it is secreted in extracellular medium from PvdRT-OpmQ efflux pump. Moreover, in PvdRT-OpmQ-deficient strains has been observed an increasing of the PVD-fluorescence in the bacterium due to PVD-metal complex formation. Other way, the presence of PvdRT-OpmQ pump, lead to decrease of PVD's fluorescence into bacteria for extrusion of PVD-metal complex compared to the control[71]. According with literature, our data showed un reduction of the fluorescence of *P. aeruginosa* strains after incubation with ZnO and Mn-ZnO which could be related to the activation of SOD and FpvA genes.

In order to evaluate the biocompatibility of Ti scaffolds dip coated with the ZnO and Mn-ZnO NPs diluted suspension (1:25, 1:50, and 1:100), we performed MTT assays on hFOB cells seeded on their surfaces, the results being shown in Fig. 7. Cell viability data demonstrate that the ZnO and Mn-ZnO coatings obtained by the 1:25 dilution significantly reduce the number of viable cells, the ZnO-covered scaffolds being extremely more cytotoxic. On the contrary, the scaffolds dip in the 1:50 and 1:100 NPs dilutions showed good biocompatibility (Fig. 7a), the percentages of viable cells against the control being (i) 19.63% for ZnO/Ti and 67.85% for Mn-ZnO/Ti at 1:25 dilution, (ii) 85.02% for ZnO/Ti and 85.19% for Mn-ZnO/Ti at 1:50 dilution, and (iii) 87.38% for ZnO/Ti and 95.84 for Mn-ZnO/Ti at 1:100 dilution.

In light of these results, we decided to perform further biocompatibility tests with prolonged times only involving the scaffolds dip in 1:50 NPs dilutions, as these also showed a good antibacterial activity (Fig. 7b). MTT results on hFOB cultured for 7 days on ZnO/Ti and Mn-ZnO/Ti from 1:50 NPs dilutions showed good biocompatibility for both metal oxides coatings compared to the control. With these coatings, the percentage of viable cells was 83.76% at D1, 77.91% at D2, and 82.69% at D7 for ZnO/Ti, while being 86.56% at D1, 93.16% at D2, and 93.59% at D7 for Mn-ZnO/Ti compared to the 100% of uncoated Ti scaffold.

The results obtained from MTT analysis displayed that both ZnO and Mn-ZnO nanocoating of Ti scaffolds at both 1:50 and and 1:100 dilutions exhibit good biocompatibility with human fetal osteoblast (hFOB) cells, in agreement with the ISO Standard 10,993–5 of 2009 for medical devices, establishing that only a cell viability reduction of more than 30% is considered cytotoxic[76]. In particular, Mn is well know to be essential in physiological processes, including bone metabolism, connective tissue development, and cell growth. Its presence could promote a more favorable cellular microenvironment for osteoblast activity and proliferation[77]. Replacing Zn with Mn in the lattice structure could modulate the surface charge, enhance protein adsorption, and improve the interaction between the scaffold and osteoblasts, further promoting cell adhesion and proliferation. Furthermore, $Mn^{2+}$ ions are involved in regulating oxidative stress responses in cells, mitigating cellular damage induced by reactive oxygen species (ROS)[33].

This is particularly relevant from a physiological perspective, as an environment conducive to the proliferation and survival of bone cells is essential for bone regeneration.

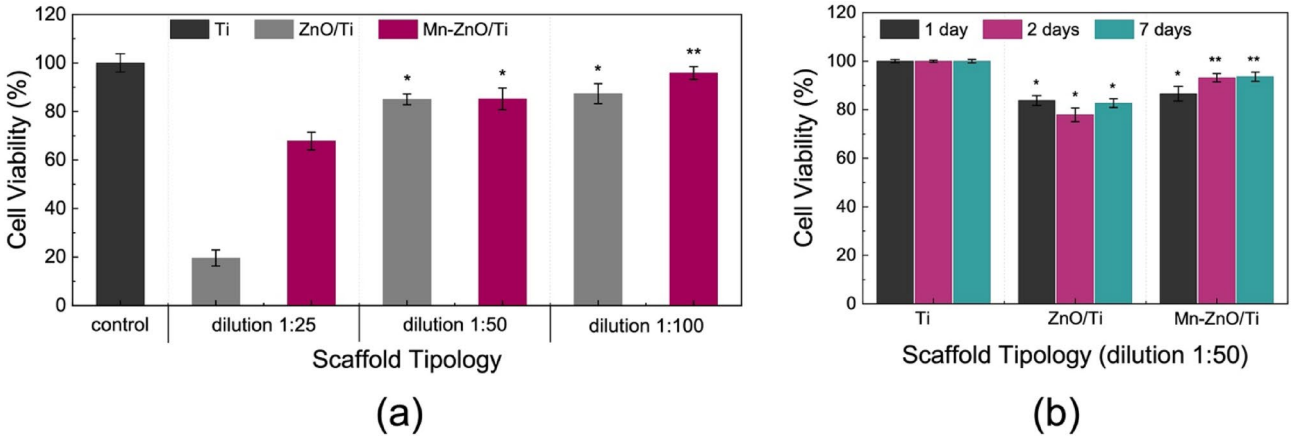


**Fig. 7**. (**a**) Cell viability assay of hFOB cells cultured on Ti, ZnO/Ti, and Mn-ZnO /Ti scaffolds coated by dipping in diluted NPs suspensions (1:25, 1:50, 1:100). (**b**) Cell viability assay of hFOB cells cultured for 1, 2, and 7 days on Ti, ZnO/Ti, and Mn-ZnO /Ti scaffolds prepared by dip coating in 50-fold diluted NPs suspensions. Data are reported as mean ± standard deviation obtained on 3 scaffolds and expressed as % of control (uncoated Ti). ANOVA test p values are reported, and $*p < 0.05$ or $**p < 0.01$ indicates significant differences between scaffolds with respect to the reference as reported by Holm post hoc test.

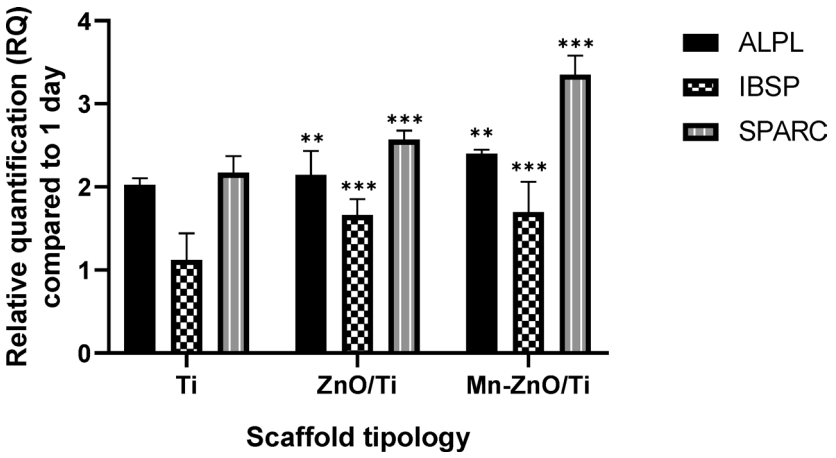


**Fig. 8**. Expression levels of osteogenic markers (ALPL, IBSP, SPARC) in hFOB cells cultured for 7 days on Ti, ZnO/Ti and Mn-ZnO/Ti scaffolds. Data are expressed as fold change from day 1. Statistical significance: $p < 0.001$ (***), $p < 0.01$ (**), compared to bare Ti.

Specifically, the 1:50 dilution coatings maintained cell viability above 80%, meeting the ISO 10,993–5 standards for medical devices. This suggests that Mn-ZnO nanoparticles not only enhance the antibacterial properties of the scaffolds but also support osteoblastic activity, promoting cell growth and proliferation without inducing significant cytotoxicity. These aspects are crucial for the clinical success of implantable biomaterials, as they facilitate effective bone integration while reducing the risk of post-operative infections.

To further investigate the osteogenic potential of the biomaterials, we performed a gene expression analysis on hFOB cells cultured on Ti, ZnO/Ti, and Mn-ZnO/Ti scaffolds up to 7 days. The relative expression of three key osteogenic differentiation markers ALPL (alkaline phosphatase), IBSP (bone sialoprotein), and SPARC (osteonectin) was assessed by qRT-PC.

As shown in Fig. 8, all three markers were significantly upregulated in cells cultured on ZnO/Ti and Mn-ZnO/Ti scaffolds compared to the uncoated Ti control. Notably, SPARC expression was most enhanced in the Mn-ZnO/Ti group, reaching approximately 3.7-fold increase versus day 1. Similarly, ALPL and IBSP were significantly upregulated on both coated scaffolds, with the highest expression levels observed in the Mn-ZnO/Ti condition. These findings indicate that the presence of ZnO and Mn-ZnO nanocoatings promotes early osteogenic commitment and matrix-related gene activation.

Collectively, the molecular data support the biocompatibility and osteo-inductive potential of the nanostructured coatings, further confirming their suitability for bone regeneration applications.

## Conclusions

The treatment of large bone defects using biomaterials exhibiting both bone tissue repair and antibacterial properties remains one of the primary targets in the current research. In this context, surface modification with inorganic NPs may represent a viable and valuable strategy. In this work, we developed ZnO and Mn-doped ZnO coatings for trabecular Ti scaffolds starting from DMSO suspension of nanoparticles having diameters of ca. 5 nm. The coatings appear uniform on the surface, as confirmed by SEM inspection. The antibacterial activity of these biomaterials was evaluated against *P. aeruginosa* (Gram negative), and *S. aureus* (Gram positive), and their biocompatibility was tested against human osteoblast cells (hFOB). Results show that the scaffolds coated through dipping in 50-fold diluted ZnO and Mn-ZnO NPs suspensions exhibit a bacterial reduction of more than 80% in the case of *S. aureus*, and of 44.4% and 53.6%, respectively, in the case of *P. aeruginosa*. A significant reduction in the pyocyanin production was also observed with *P. aeruginosa,* indicating that the metabolism of the Gram-negative strain was significantly altered with a relevant impact on bacterial growth, although the presence of $Zn^{2+}$ and $Mn^{2+}$ ions was not sufficient to reduce drastically the bacterial load on the Ti surface. An *in-silico* analysis highlighted the genes involved in the two metal ions resistance for both *S. aureus* and *P. aeruginosa* that will be experimentally investigated in future work. Parallel biocompatibility results showed that Ti scaffolds coated with ZnO and Mn-ZnO from the 1:50 diluted suspensions exhibit good biocompatibility in agreement with the ISO Standard 10,993–5 of 2009 for medical devices. Furthermore, gene expression analysis of osteogenic markers confirmed the ability of Mn-ZnO coatings to promote early osteogenic differentiation, supporting the physiological relevance of these materials in bone regeneration contexts.

The presented coated scaffolds would find their place in tissue engineering as templates for cellular interaction, providing support to native tissue and possibly incorporating essential growth factors to control and enhance normal physiological tissue growth development.

Overall, the presented results indicate that the nanocoatings here described are effective in providing scaffolds with antibacterial and osteo-integrative properties without relevant citotoxity aspects. However some future studies are needed to gain insight on the biocompatibility aspect overcoming the current limitations. In particular, long-term in vivo stability, immune response, and systemic effects have not been explored. Biological interactions with complex environments, such as bone marrow and extracellular matrices, should also be explored to assess biointegration and tissue regeneration over time. Furthermore, scaling up the synthesis and coating processes may present challenges.

Future work will be devoted to further investigation on molecular pathways involved in cell proliferation, bone matrix formation, and bacterial death, togheter with the in vivo study to further assess biointegration and optimize clinical translation in order to pave the way for a new class of biomaterials for regenerative medicine applications and implantable devices.

## Methods

### Chemicals

Zn(II) acetate dihydrate, Mn(II) acetate tetrahydrate, dimethyl sulfoxide (DMSO, HPLC grade), tetramethylammonium hydroxide (25 wt%), hydrogen peroxide (30% v/v), ammonium hydroxide (30% v/v), and ultra-pure water (UPW) were purchased by Sigma-Aldrich.

### ZnO and Mn-ZnO NPs synthesis

The synthesis of zinc oxide nanoparticles (ZnO NPs) was performed by chemical synthesis in solution according to the approach described by Panasiuk et al.[78]. In agreement with our previous work[37], ZnO and Mn-doped-ZnO (Mn-ZnO) NPs were synthesized. Specifically, 19.7 mL of a $Zn(CH_3COO)_2{\cdot}2H_2O$ solution in DMSO ($[Zn^{2+}] = 0.2$ M) is rapidly added by 3 mL of an aqueous solution of $N(CH_3)_4OH$ (25% w/w) in a $[Zn^{2+}]:[OH^-] = 1:2$ molarity ratio at room temperature (RT), the solution immediately turning a milky-white color. The suspension was left under stirring for 30 min at RT. The purification was carried out by three 10-min centrifugation cycles at 5000 rpm, and the white solid was resuspended in DMSO, obtaining a ZnO concentration of about 16.3 mg/mL.

The synthesis of manganese-doped zinc oxide nanoparticles (Mn-ZnO NPs) was as follows: 20 mL of a DMSO solution containing $Zn(CH_3COO)_2{\cdot}2H_2O$ and $Mn(CH_3COO)_2{\cdot}4H_2O$ (total metal ions molarity $[M^{2+}] = 0.2$ M; ions molarity ratio $[Zn^{2+}]:[Mn^{2+}] = 0.975{:}0.25$) were prepared and rapidly added of an aqueous solution of $N(CH_3)_4OH$ (25% w/w, 3 mL), with a $[M^{2+}]:[OH^-] = 1:2$ molarity ratio at RT. The solution immediately turned an opaque brown color, leaving the suspension under stirring for 30 min at RT. The purification was carried out by three 10-min centrifugation cycles at 5000 rpm, and the brown solid was resuspended in DMSO, obtaining a Mn-ZnO concentration of about 16.3 mg/mL. 25-, 50-, and 100-fold dilutions were prepared from the stock suspensions, obtaining 652 µg/mL, 326 µg/mL, and 163 µg/mL suspensions of monodispersed nanoparticles in DMSO, respectively.

### ZnO NPs and Mn-ZnO NPs deposition onto Ti scaffolds

ZnO and Mn-ZnO NPs were deposited onto $1 \times 1 \times 0.26$ $cm^3$ trabecular titanium scaffolds (see figure S4-a) made up of a Ti-6Al-4 V alloy. The scaffolds were cleaned by immersion in a basic piranha solution consisting of a 2:1:1 v/v mixture of $H_2O$, $H_2O_2$ (30 wt%), and $NH_4OH$ (30 wt%). This process was carried out at about 80 °C under stirring for 10 min. Then, the cleaned substrates were washed thoroughly with deionized (DI) water.

Subsequently, the scaffolds were dipped in the 652 µg/mL, 326 µg/mL, and 163 µg/mL ZnO or Mn-ZnO NPs suspensions for 2 s and dried at 50 °C (figure S4-b), performing three cycles of dipping with the ZnO NPs suspension and two cycles with the Mn-ZnO NPs, these conditions yielding a uniform coverage of the scaffolds' surface. The samples were washed thrice by immersion in deionized water at 37 °C inside an incubator with constant and gentle oscillation.

This method is scalable to real prostheses of any dimensions ad shapes, and compatible with current industrial processes.

### Transmission electron microscopy (TEM), energy dispersive X-ray (EDX), and electron energy loss spectroscopy (EELS) characterization

Concerning TEM/EDX/EELS characterization, ZnO and Mn-ZnO NPs suspensions were dripped onto a gold grid with a thin lacey carbon film and vacuum dried for 24 h. TEM analyses were performed on a JEOL ARM200F equipped with a cold Field Emission electron Gun (CFEG) and a spherical aberration corrector able to deliver a spatial resolution of 0.6 Å. The chemical analysis was carried out through a 100 $mm^2$ energy dispersive X-ray detector (EDX) and a post-column GATAN Electron Energy loss Spectrometer (EELS) able to work in dual EELS mode to allow a precise measurement of the energy loss with a resolution down to 0.3 eV. The images were analyzed by using the Gatan and ImageJ softwares.

### FT-IR characterization

Infrared absorption measurements of the ZnO and Mn-doped ZnO nanoparticle suspension were carried out in the 4000–650 $cm^{-1}$ range using a Fourier transform infrared (FT-IR) Perkin-Elmer spectrophotometer (Spectrum 100 model).

### Scanning electron microscopy (SEM) and energy dispersive X-ray (EDX) characterization

A Merlin model ZEISS Gemini 2 instrument (primary voltage = 30 kV and 150 kV) was used to perform scanning electron microscopy (SEM) measures on the hybrid NPs/Ti biomaterials. Energy dispersive X-ray (EDX) data was analyzed by a Quantax EDX spectrometer. The EDX-detected pear-shaped dimension is about 0.7 μm.

## Evaluation of the antibacterial activity

*Pseudomonas aeruginosa* ATCC27853 and *Staphylococcus aureus* ATCC29213 were purchased from the American Type Culture Collection (LGC Promochem, Milan, Italy) and cultured in Luria–Bertani broth (LB, Sigma-Aldrich, Milan) and tryptone soy broth (TSB, Sigma-Aldrich, Milan), respectively. Each strain was maintained in the respective medium according to two different storage protocols, i.e., short- and long-term. Short-term storage aimed to provide active bacterial cultures readily available for daily use. For this purpose, plate culture triplicates (work plates) were prepared for each strain and stored at 4 °C weekly. At the same time, cryopreservation (at -80 °C) of the bacterial strains was performed by adding sterile glycerol (final concentration: 20% v/v) to liquid cultures in a stationary phase for long-term storage. Overall, the chosen protocols mainly aimed to maintain the vitality and genetic stability of the different bacterial species under study.

The antibacterial action mediated by the different coatings was evaluated on free-floating (planktonic) and adhered (sessile) cells. For this purpose, standardized suspensions from each bacterial strain were prepared as follows: 1–2 colonies were picked off a work plate, entirely suspended in 5 mL medium in 50 mL tubes and incubated under shaking at 37 °C until reaching a 0.2 optical density at 540 nm ($OD_{540}$), corresponding to about $10^8$ bacteria/mL. Then, this bacterial culture was serially diluted in fresh medium to obtain a suspension of $10^5$ bacteria /mL and subsequently aliquoted in 24-well plates (2 mL/well). Each well was added with uncoated (Ti), ZnO NPs-coated (ZnO/Ti), and Mn-ZnO NPs-coated (Mn-ZnO/Ti) titanium scaffolds, previously decontaminated by exposure to UV-C for 1 h. The so-prepared plate was incubated under gentle shaking (100 rpm, orbital shaker KS-15, Edmund Bühler GmbH) overnight (18 h) at 37 °C.

After incubation, the antibacterial action of the different coatings was evaluated on planktonic and sessile cells. The growth of planktonic cells was evaluated via turbidimetry using a synergy HT plate reader (BioTek Instruments, Inc., VT, United States), whereas sessile cells were evaluated through previously optimized protocols[37]. Specifically, Ti scaffolds were aseptically transferred into a new 24-well plate, washed thrice with phosphate buffer saline (PBS), and placed in 15 mL tubes containing 1 mL of PBS. The strongly adhering sessile bacteria were mechanically detached from the scaffolds by vortexing for 60 s and quantified by the Colony Forming Units (CFU) assay[79].

### In silico analysis of genes involved in bacterial resistance to Zn and Mn ions

The antibacterial biocide and metal resistance genes, BacMet, database was used to identify the genes that could be involved in the bacterial resistance to metal ions. BacMet is a gene bank that collects 470 experimentally verified resistance genes organized according to their molecular function and induced resistance phenotype. In addition, the database includes 25.477 potential resistance genes collected from public sequence repositories[80]. Firstly, the results were individually filtered for the $Zn^{2+}$ and $Mn^{2+}$ metal ions and then evaluated for the bacterial strains under study.

### Cell culture and viability assay

Human fetal osteoblast cell line hFOB 1.19 was obtained from the American Type Culture Collection (ATCC, Manassas, VA, USA). hFOB 1.19 was cultured in 1:1 mixture of Ham's F12 Medium—Dulbecco's Modified Eagle's Medium (D8437, Merk Life Science S.r.l., Milan, Italy), supplemented with 2.5 mM L-glutamine (G7513, Merk Life Science S.r.l., Milan, Italy), 0.3 mg/mL G418 (4,727,878,001, Merk Life Science S.r.l., Milan, Italy), 10% Foetal Bovine Serum (F7524, FBS, Merk Life Science S.r.l., Milan, Italy), and incubated at 37 °C in a humidified atmosphere containing 5% $CO_2$. The medium was replaced twice a week, and cells were split at about 80% of confluence.

Before the in vitro studies, the Ti, ZnO/Ti and Mn-ZnO/Ti scaffolds were sterilized under UV light for 2 h. Cell viability of hFOB cells cultured on Ti, ZnO/Ti, and Mn-ZnO/Ti scaffolds was tested by MTT [3-(4,5-dimethylthia-zol-2-yl)-2,5-diphenyltetrazolium bromide] assay (M2128, Merk Life Science S.r.l., Milan,

| Protein name | Target gene | Forward | Reverse |
|---|---|---|---|
| Glyceraldehyde 3-phosphate dehydrogenase | GAPDH | AACAGCGACACCCACTCCTC | CATACCAGGAAATGAGCTTGACAA |
| Alkalinephosphatase | ALP | ACCATTCCCACGTCTTCACATTT | AGACATTCTCTCGTTCACCGCC |
| Osteonectin | SPARC | TGCCTGATGAGACAGAGGTGGT | CTTCGGTTTCCTCTGCACCATC |
| Bone Sialoprotein | IBSP | GGCAGTAGTGACTCATCCGAAG | GAAAGTGTGGTATTCTCAGCCTC |

**Table 2**. Primer sequences.

Italy). Specifically, $1 \times 10^6$ cells suspended in 50 µL of culture medium were slowly drop-seeded on Ti, ZnO/Ti, and Mn-ZnO/Ti scaffolds in 24-well culture plates and incubated at 37 °C in a humidified atmosphere containing 5% $CO_2$ for 4 h. Successively, the medium was added up to cover the scaffolds and incubated for 1, 2 and 6 days. At the end of each time point, the culture medium was removed from each well, replaced with MTT solution (1 mg/mL in FBS-free medium), and incubated at 37 °C in a humidified atmosphere containing 5% $CO_2$ for 2 h. Then, the MTT solution was removed from each well, and the formazan crystals were dissolved using DMSO (A3672,0250, PanReac AppliChem, ITW Reagents, S.R.L., Monza, Italy). The absorbance at 540 nm was read using a microplate reader (VT, USA). The cells cultured on the Ti scaffold were used as a control for determining cell viability.

### Gene expression analysis of osteogenic markers

The expression of osteogenic differentiation markers was evaluated in hFOB cells cultured on Ti, ZnO/Ti, and Mn-ZnO/Ti scaffolds for 7 days. Total RNA was extracted using Trizol Reagent (Life Technologies, Carlsbad, CA, USA), following the manufacturer's protocol. Quantitative real-time PCR (qRT-PCR) was conducted using the 7500 Fast Real-Time PCR System (Applied Biosystems) in a 20 µL reaction mixture consisting of 1 µL of cDNA, 0.5 µM of each forward and reverse primer, and 10 µL of SsoAdvanced Universal SYBR® Green Supermix 2 × (Bio-Rad Laboratories, Hercules, CA, USA). Gene expression levels were calculated using the $2^{-\Delta\Delta Ct}$ method, with *GAPDH* as the internal control. Data were expressed as fold change relative to day 1. Primer sequences used for *ALPL*, *IBSP*, *SPARC*, and *GAPDH* are reported in Table 2.

### Statistical analysis

All samples were analyzed in triplicate. Data were analyzed as mean ± standard error (SE) and expressed as percentages versus uncoated scaffolds (Ti). ANOVA test $p$ values are reported, with $^*p < 0.05$ or $^{**}p < 0.01$ indicating significant differences between scaffolds as reported by the Holm post hoc test.

## Data availability

The datasets used and/or analysed during the current study available from the corresponding author on reasonable request.

Received: 1 August 2024; Accepted: 25 June 2025
Published online: 15 October 2025

## References

1. Babuska, V. et al. Nanomaterials in bone regeneration. *Appl. Sci.* **12**, 6793 (2022).
2. Laurencin, C. T., Ambrosio, A. M. A., Borden, M. D. & Cooper, J. A. Tissue engineering: Orthopedic applications. *Annu. Rev. Biomed. Eng.* **1**, 19–46 (1999).
3. Laurencin, C., Khan, Y. & El-Amin, S. F. Bone graft substitutes. *Expert Rev. Med. Dev.* **3**(1), 49–57 (2006).
4. Baroli, B. From natural bone grafts to tissue engineering therapeutics: Brainstorming on pharmaceutical formulative requirements and challenges. *J. Pharm. Sci.* **98**, 1317–1375 (2009).
5. Dimitriou, R., Jones, E., McGonagle, D. & Giannoudis, P. V. Bone regeneration: Current concepts and future directions. *BMC Med.* **9**, 66 (2011).
6. Shi, J.-J. et al. Graphene oxide-modified layered double hydroxide/chitosan nacre-mimetic scaffolds treat breast cancer metastasis-induced bone defects. *Carbon* **200**, 63–74 (2022).
7. Gao, C., Peng, S., Feng, P. & Shuai, C. Bone biomaterials and interactions with stem cells. *Bone Res.* **5**(1), 1–33 (2017).
8. Franco, D. et al. Biological response evaluation of human fetal osteoblast cells and bacterial cells on fractal silver dendrites for bone tissue engineering. *Nanomaterials* **13**, 1107 (2023).
9. Rizzo, M. G. et al. Physiologic response evaluation of human foetal osteoblast cells within engineered 3D-printed polylactic acid scaffolds. *Biology* **12**, 424 (2023).
10. Ahmed, W., Zhai, Z. & Gao, C. Adaptive antibacterial biomaterial surfaces and their applications. *Mater. Today Bio.* **2**, 100017 (2019).
11. Wang, M. & Tang, T. Surface treatment strategies to combat implant-related infection from the beginning. *J. Orthop. Translat.* **17**, 42–54 (2018).
12. Dong, J. et al. Immunomodulatory biomaterials for implant-associated infections: From conventional to advanced therapeutic strategies. *Biomater. Res.* **26**, 72 (2022).
13. Liang, S. X. et al. Development of a new β Ti alloy with low modulus and favorable plasticity for implant material. *Mater. Sci. Eng., C* **61**, 338–343 (2016).
14. Long, M. & Rack, H. J. Titanium alloys in total joint replacement—A materials science perspective. *Biomaterials* **19**, 1621–1639 (1998).
15. Attarilar, S., Salehi, M. T., Al-Fadhalah, K. J., Djavanroodi, F. & Mozafari, M. Functionally graded titanium implants: Characteristic enhancement induced by combined severe plastic deformation. *PLoS ONE* **14**, e0221491 (2019).
16. Zhu, W. et al. Enhanced corrosion resistance of zinc-containing nanowires-modified titanium surface under exposure to oxidizing microenvironment. *J. Nanobiotechnol.* **17**, 55 (2019).

17. Malhotra, R. et al. Inhibiting corrosion of biomedical-grade Ti-6Al-4V alloys with graphene nanocoating. *J. Dent. Res.* **99**, 285–292 (2020).
18. Lei, T. et al. Silicon-incorporated nanohydroxyapatite-reinforced poly(ε-caprolactone) film to enhance osteogenesis for bone tissue engineering applications. *Colloids Surf., B* **187**, 110714 (2020).
19. Zhu, C. et al. Proliferation and osteogenic differentiation of rat BMSCs on a novel Ti/SiC metal matrix nanocomposite modified by friction stir processing. *Sci. Rep.* **6**, 38875 (2016).
20. Levin, M., Spiro, R. C., Jain, H. & Falk, M. M. Effects of titanium implant surface topology on bone cell attachment and proliferation in vitro. *Med. Dev.: Evid. Res.* **15**, 103–119 (2022).
21. Tong, S. Y. C. et al. *Staphylococcus aureus* infections: Epidemiology, pathophysiology, clinical manifestations, and management. *Clin. Microbiol. Rev.* **28**, 603 (2015).
22. Chouirfa, H., Bouloussa, H., Migonney, V. & Falentin-Daudré, C. Review of titanium surface modification techniques and coatings for antibacterial applications. *Acta Biomater.* **83**, 37–54 (2019).
23. Liu, J. et al. Nano-modified titanium implant materials: A way toward improved antibacterial properties. *Front. Bioeng. Biotechnol.* **8**, 576969 (2020).
24. Vimbela, G. V., Ngo, S. M., Fraze, C., Yang, L. & Stout, D. A. Antibacterial properties and toxicity from metallic nanomaterials. *Int. J. Nanomed.* **12**, 3941–3965 (2017).
25. Shabatina, T. I., Vernaya, O. I. & Melnikov, M. Y. Hybrid nanosystems of antibiotics with metal nanoparticles-novel antibacterial agents. *Molecules* **28**, 1603 (2023).
26. Godoy-Gallardo, M. et al. Antibacterial approaches in tissue engineering using metal ions and nanoparticles: From mechanisms to applications. *Bioactive Mater.* **6**, 4470–4490 (2021).
27. Ishida, T. Antibacterial mechanism of Ag+ ions for bacteriolyses of bacterial cell walls via peptidoglycan autolysins, and DNA damages. *MOJ Toxicol.* https://doi.org/10.15406/MOJT.2018.04.00125 (2018).
28. Nakamura, H. & Watano, S. Direct permeation of nanoparticles across cell membrane: A review. *KONA Powder Particle J.* **2018**, 49–65 (2018).
29. Wang, L. et al. Morphology-dependent bactericidal activities of Ag/$CeO_2$ catalysts against *Escherichia coli*. *J. Inorg. Biochem.* **135**, 45–53 (2014).
30. Qi, K., Cheng, B., Yu, J. & Ho, W. Review on the improvement of the photocatalytic and antibacterial activities of ZnO. *J. Alloys Compd.* **727**, 792–820 (2017).
31. Su, Y. et al. Zinc-based biomaterials for regeneration and therapy. *Trends Biotechnol.* **37**, 428–441 (2019).
32. Gnaneshwar, P. V. et al. Ramification of zinc oxide doped hydroxyapatite biocomposites for the mineralization of osteoblasts. *Mater. Sci. Eng., C* **96**, 337–346 (2019).
33. Yu, Z. et al. Reactive oxygen species-related nanoparticle toxicity in the biomedical field. *Nanoscale Res. Lett.* **15**, 115 (2020).
34. Alloway, B. J. Heavy metals and metalloids as micronutrients for plants and animals. In *Heavy metals in soils: Trace metals and metalloids in soils and their bioavailability* (ed. Alloway, B. J.) 195–209 (Springer Netherlands, Dordrecht, 2013). https://doi.org/10.1007/978-94-007-4470-7_7.
35. Li, L. & Yang, X. The essential element manganese, oxidative stress, and metabolic diseases: Links and interactions. *Oxid. Med. Cell. Longev.* **2018**, e7580707 (2018).
36. Klimis-Zacas, D. *Manganese in health and disease* (CRC Press, 1993).
37. Calabrese, G. et al. Structural and antibacterial studies of novel ZnO and ZnxMn(1–x)O nanostructured titanium scaffolds for biomedical applications. *Biomater. Adv.* **145**, 213193 (2023).
38. Fakhari, S., Jamzad, M. & Kabiri Fard, H. Green synthesis of zinc oxide Nanoparticles: A comparison. *Green Chem. Lett. Rev.* **12**, 19–24 (2019).
39. Loomer, D. B., Al, T. A., Weaver, L. & Cogswell, S. Manganese valence imaging in Mn minerals at the nanoscale using STEM-EELS. *Am. Miner.* **92**, 72–79 (2007).
40. Elilarassi, R. & Chandrasekaran, G. Structural, optical and magnetic properties of nanoparticles of ZnO:Ni—DMS prepared by sol–gel method. *Mater. Chem. Phys.* **123**, 450–455 (2010).
41. Gao, Q. et al. Effects of Mn dopant on tuning carrier concentration in Mn doped ZnO nanoparticles synthesized by co-precipitation technique. *J. Mater. Sci.: Mater. Electron.* **29**, 3568–3575 (2018).
42. Shatnawi, M. et al. Influence of Mn doping on the magnetic and optical properties of ZnO nanocrystalline particles. *Results Phys.* **6**, 1064–1071 (2016).
43. Karamat, S. et al. Structural, optical and magnetic properties of (ZnO)1–x($MnO_2$)x thin films deposited at room temperature. *Appl. Surf. Sci.* **254**, 7285–7289 (2008).
44. Saw, K. G., Aznan, N. M., Yam, F. K., Ng, S. S. & Pung, S. Y. New Insights on the burstein-moss shift and band gap narrowing in indium-doped zinc oxide thin films. *PLoS ONE* **10**, e0141180 (2015).
45. Yogamalar, N. R. & Chandra Bose, A. Burstein-Moss shift and room temperature near-band-edge luminescence in lithium-doped zinc oxide. *Appl. Phys. A* **103**, 33–42 (2011).
46. Fernandes, A. & Dias, M. The microbiological profiles of infected prosthetic implants with an emphasis on the organisms which form biofilms. *J. Clin. Diagn. Res.* **7**, 219–223 (2013).
47. Visperas, A., Santana, D., Klika, A. K., Higuera-Rueda, C. A. & Piuzzi, N. S. Current treatments for biofilm-associated periprosthetic joint infection and new potential strategies. *J. Orthop. Res.* **40**, 1477–1491 (2022).
48. Santos, V. L., Nardi Drummond, R. M. & Dias-Souza, M. V. Biosurfactants as Antimicrobial and Antibiofilm Agents. In *Current Developments in Biotechnology and Bioengineering* (eds. Thomaz-Soccol, V., Pandey, A. & Resende, R. R.) 371–402 (Elsevier, 2017). https://doi.org/10.1016/B978-0-444-63660-7.00015-2.
49. Cheng, Y., Feng, G. & Moraru, C. I. Micro- and nanotopography sensitive bacterial attachment mechanisms: A review. *Front. Microbiol.* **10**, 191 (2019).
50. Sharma, D., Misba, L. & Khan, A. U. Antibiotics versus biofilm: An emerging battleground in microbial communities. *Antimicrob. Resist. Infect. Control* **8**, 76 (2019).
51. Pierson, L. S. & Pierson, E. A. Metabolism and function of phenazines in bacteria: Impacts on the behavior of bacteria in the environment and biotechnological processes. *Appl. Microbiol. Biotechnol.* **86**, 1659–1670 (2010).
52. Rodriguez-Urretavizcaya, B. et al. Diagnosis and stratification of *Pseudomonas aeruginosa* infected patients by immunochemical quantitative determination of pyocyanin from clinical bacterial isolates. *Front. Cell Infect. Microbiol.* **11**, 786929 (2021).
53. Tuon, F. F., Dantas, L. R., Suss, P. H. & Tasca Ribeiro, V. S. Pathogenesis of the *Pseudomonas aeruginosa* biofilm: A review. *Pathogens* **11**, 300 (2022).
54. Costa, K. C., Glasser, N. R., Conway, S. J. & Newman, D. K. Pyocyanin degradation by a tautomerizing demethylase inhibits *Pseudomonas aeruginosa* biofilms. *Science* **355**, 170–173 (2017).
55. Yu, J. M., Wang, D., Pierson, L. S. & Pierson, E. A. Effect of producing different phenazines on bacterial fitness and biological control in *Pseudomonas chlororaphis* 30–84. *Plant Pathol. J.* **34**, 44–58 (2018).
56. Abdelaziz, A. A., Kamer, A. M. A., Al-Monofy, K. B. & Al-Madboly, L. A. *Pseudomonas aeruginosa*'s greenish-blue pigment pyocyanin: Its production and biological activities. *Microb. Cell Fact.* **22**, 1–14 (2023).
57. Vetrivel, A. et al. *Pseudomonas aeruginosa* biofilm formation and its control. *Biologics* **1**, 312–336 (2021).
58. Lee, J. & Zhang, L. The hierarchy quorum sensing network in *Pseudomonas aeruginosa*. *Protein Cell* **6**, 26–41 (2015).

59. Ali, S. G. et al. Effect of biosynthesized ZnO nanoparticles on multi-drug resistant *Pseudomonas aeruginosa*. *Antibiotics* **9**, 260 (2020).
60. Al-Shabib, N. A. et al. Biogenic synthesis of Zinc oxide nanostructures from Nigella sativa seed: Prospective role as food packaging material inhibiting broad-spectrum quorum sensing and biofilm. *Sci. Rep.* **6**, 36761 (2016).
61. Gudkov, S. V. et al. A mini review of antibacterial properties of ZnO nanoparticles. *Front. Phys.* **9**, 641481 (2021).
62. Mendes, C. R. et al. Antibacterial action and target mechanisms of zinc oxide nanoparticles against bacterial pathogens. *Sci. Rep.* **12**, 2658 (2022).
63. Saod, W. M., Hamid, L. L., Alaallah, N. J. & Ramizy, A. Biosynthesis and antibacterial activity of manganese oxide nanoparticles prepared by green tea extract. *Biotechnol. Rep.* **34**, e00729 (2022).
64. Berendonk, T. U. et al. Tackling antibiotic resistance: The environmental framework. *Nat. Rev. Microbiol.* **13**, 310–317 (2015).
65. Endo, G. & Silver, S. CadC, the transcriptional regulatory protein of the cadmium resistance system of *Staphylococcus aureus* plasmid pI258. *J. Bacteriol.* **177**, 4437–4441 (1995).
66. Crupper, S. S., Worrell, V., Stewart, G. C. & Iandolo, J. J. Cloning and expression of cadD, a new cadmium resistance gene of *Staphylococcus aureus*. *J. Bacteriol.* **181**, 4071–4075 (1999).
67. Kuroda, M. et al. Whole genome sequencing of meticillin-resistant *Staphylococcus aureus*. *Lancet* **357**, 1225–1240 (2001).
68. Valencia, E. Y., Braz, V. S., Guzzo, C. & Marques, M. V. Two RND proteins involved in heavy metal efflux in Caulobacter crescentus belong to separate clusters within proteobacteria. *BMC Microbiol.* **13**, 79 (2013).
69. Hassan, M. T. et al. Identification of a gene cluster, czr, involved in cadmium and zinc resistance in *Pseudomonas aeruginosa*. *Gene* **238**, 417–425 (1999).
70. Kuroda, M., Hayashi, H. & Ohta, T. Chromosome-determined zinc-responsible operon czr in *Staphylococcus aureus* strain 912. *Microbiol. Immunol.* **43**, 115–125 (1999).
71. Hannauer, M. et al. The PvdRT-OpmQ efflux pump controls the metal selectivity of the iron uptake pathway mediated by the siderophore pyoverdine in *Pseudomonas aeruginosa*. *Environ. Microbiol.* **14**, 1696–1708 (2012).
72. Hassett, D. J. et al. Cloning and characterization of the *Pseudomonas aeruginosa* sodA and sodB genes encoding manganese- and iron-cofactored superoxide dismutase: Demonstration of increased manganese superoxide dismutase activity in alginate-producing bacteria. *J. Bacteriol.* **175**, 7658–7665 (1993).
73. Horsburgh, M. J., Clements, M. O., Crossley, H., Ingham, E. & Foster, S. J. PerR controls oxidative stress resistance and iron storage proteins and is required for virulence in *Staphylococcus aureus*. *Infect. Immun.* **69**, 3744–3754 (2001).
74. Hoogewerf, A. J. et al. Functional characterization of a cadmium resistance operon in Staphylococcus aureus ATCC12600: CadC does not function as a repressor. *J. Basic Microbiol.* **55**, 148–159 (2015).
75. Hassett, D. J., Schweizer, H. P. & Ohman, D. E. *Pseudomonas aeruginosa* sodA and sodB mutants defective in manganese- and iron-cofactored superoxide dismutase activity demonstrate the importance of the iron-cofactored form in aerobic metabolism. *J. Bacteriol.* **177**, 6330–6337 (1995).
76. Al-Zyoud, W., Haddadin, D., Hasan, S. A., Jaradat, H. & Kanoun, O. Biocompatibility testing for implants: A novel tool for selection and characterization. *Materials* **16**, 6881 (2023).
77. Taskozhina, G., Batyrova, G., Umarova, G., Issanguzhina, Z. & Kereyeva, N. The manganese-bone connection: Investigating the role of manganese in bone health. *J. Clin. Med.* **13**, 4679 (2024).
78. Panasiuk, Y. V. et al. Colloidal ZnO nanocrystals in dimethylsulfoxide: A new synthesis, optical, photo- and electroluminescent properties. *Nanotechnology* **25**, 075601 (2014).
79. Zagami, R. et al. Sulfobutylether-β-cyclodextrin/5,10,15,20-tetrakis(1-methylpyridinium-4-yl)porphine nanoassemblies with sustained antimicrobial phototherapeutic action. *Int. J. Pharm.* **585**, 119487 (2020).
80. Pal, C., Bengtsson-Palme, J., Rensing, C., Kristiansson, E. & Larsson, D. G. J. BacMet: Antibacterial biocide and metal resistance genes database. *Nucleic Acids Res.* **42**, D737-743 (2014).


## Author contributions

M.D. and D.F. and M.G.R. carried out experimental work and data curation; M.L.D.P set up methodology and data analysis; M.G and I.A contribute to the experimental work; G.C. and M.S.N. set up methodology and support the data analysis; G.D.L give conceptualization, supervision review and editing the manuscript; C.C., E.F and F.N., A.A.L.and G.N. set up methodology and carried out data analysis; S.C. give conceptualization, supervision, writing, review and editing the manuscript;

## Funding

This research was partially funded by the Italian Ministry of Economics—Project MISE ORTHO Line: *Development of a Production Line for Implantable Medical Devices*—Prog. n. F/190169/01—03/X44.

## Declarations

## Competing interest

The authors declare no competing interests.

## Additional information

**Supplementary Information** The online version contains supplementary material available at https://doi.org/10.1038/s41598-025-09058-z.

**Correspondence** and requests for materials should be addressed to G.L. or S.C.